Measurement of resolved resonances of ^{232}Th(n, γ) at the n_TOF facility at CERN

F. Gunsing,[1,*] E. Berthoumieux,[1] G. Aerts,[1] U. Abbondanno,[2] H. Álvarez,[3] F. Alvarez-Velarde,[4] S. Andriamonje,[1] J. Andrzejewski,[5] P. Assimakopoulos,[6] L. Audouin,[7] G. Badurek,[8] P. Baumann,[9] F. Bečvář,[10] F. Calviño,[11] D. Cano-Ott,[4] R. Capote,[12,13] A. Carrillo de Albornoz,[14] P. Cennini,[15] V. Chepel,[16] E. Chiaveri,[15] N. Colonna,[17] G. Cortes,[11] A. Couture,[18] J. Cox,[18] M. Dahlfors,[15] S. David,[9] I. Dillman,[19] R. Dolfini,[20] C. Domingo-Pardo,[21] W. Dridi,[1] I. Duran,[3] C. Eleftheriadis,[22] M. Embid-Segura,[4] L. Ferrant,[7] A. Ferrari,[15] R. Ferreira-Marques,[16] L. Fitzpatrick,[15] H. Frais-Koelbl,[23] K. Fujii,[2] W. Furman,[24] I. Goncalves,[16] E. Gonzalez-Romero,[4] A. Goverdovski,[25] F. Gramegna,[26] E. Griesmayer,[23] C. Guerrero,[4] B. Haas,[27] R. Haight,[28] M. Heil,[19] A. Herrera-Martinez,[15] M. Igashira,[29] S. Isaev,[7] E. Jericha,[8] F. Käppeler,[19] Y. Kadi,[15] D. Karadimos,[6] D. Karamanis,[6] M. Kerveno,[9] V. Ketlerov,[15,25] P. Koehler,[30] V. Konovalov,[15,24] E. Kossionides,[31] M. Krtička,[10] C. Lampoudis,[22] H. Leeb,[8] A. Lindote,[16] I. Lopes,[16] M. Lozano,[13] S. Lukic,[9] J. Marganiec,[5] L. Marques,[14] S. Marrone,[17] P. Mastinu,[26] A. Mengoni,[15,23] P. M. Milazzo,[2] C. Moreau,[2] M. Mosconi,[19] F. Neves,[16] H. Oberhummer,[8] S. O'Brien,[18] M. Oshima,[32] J. Pancin,[1] C. Papachristodoulou,[6] C. Papadopoulos,[33] C. Paradela,[3] N. Patronis,[6] A. Pavlik,[34] P. Pavlopoulos,[35] L. Perrot,[1] M. T. Pigni,[8] R. Plag,[19] A. Plompen,[36] A. Plukis,[1] A. Poch,[11] C. Pretel,[11] J. Quesada,[13] T. Rauscher,[37] R. Reifarth,[28] M. Rosetti,[38] C. Rubbia,[20] G. Rudolf,[9] P. Rullhusen,[36] J. Salgado,[14] L. Sarchiapone,[15] I. Savvidis,[22] C. Stephan,[7] G. Tagliente,[17] J. L. Tain,[21] L. Tassan-Got,[7] L. Tavora,[14] R. Terlizzi,[17] G. Vannini,[39] P. Vaz,[14] A. Ventura,[38] D. Villamarin,[4] M. C. Vincente,[4] V. Vlachoudis,[15] R. Vlastou,[33] F. Voss,[19] S. Walter,[19] H. Wendler,[15] M. Wiescher,[18] and K. Wisshak[19]

(n_TOF Collaboration[†])

[1]*CEA/Saclay—DSM/Irfu/SPhN, F-91191 Gif-sur-Yvette, France*

[2]*Istituto Nazionale di Fisica Nucleare, Trieste, Italy*

[3]*Universidade de Santiago de Compostela, Spain*

[4]*Centro de Investigaciones Energeticas Medioambientales y Technologicas, Madrid, Spain*

[5]*University of Lodz, Lodz, Poland*

[6]*University of Ioannina, Ioannina, Greece*

[7]*Centre National de la Recherche Scientifique/IN2P3—IPN, Orsay, France*

[8]*Atominstitut der Österreichischen Universitäten, Technische Universität Wien, Wien, Austria*

[9]*Centre National de la Recherche Scientifique/IN2P3—IReS, Strasbourg, France*

[10]*Charles University, Prague, Czech Republic*

[11]*Universitat Politecnica de Catalunya, Barcelona, Spain*

[12]*International Atomic Energy Agency, NAPC/Nuclear Data Section, Vienna, Austria*

[13]*Universidad de Sevilla, Sevilla, Spain*

[14]*Instituto Tecnológico e Nuclear (ITN), Lisbon, Portugal*

[15]*CERN, Geneva, Switzerland*

[16]*LIP—Coimbra & Departamento de Fisica da Universidade de Coimbra, Coimbra, Portugal*

[17]*Istituto Nazionale di Fisica Nucleare, Bari, Italy*

[18]*University of Notre Dame, Notre Dame, Indiana, USA*

[19]*Karlsruhe Institute for Technology (KIT), Campus North, P.O. Box 3640, 76021 Karlsruhe, Germany*

[20]*Università degli Studi Pavia, Pavia, Italy*

[21]*Instituto de Física Corpuscular, CSIC—Universidad de Valencia, Valencia, Spain*

[22]*Aristotle University of Thessaloniki, Thessaloniki, Greece*

[23]*International Atomic Energy Agency (IAEA), Nuclear Data Section, Vienna, Austria*

[24]*Joint Institute for Nuclear Research, Frank Laboratory of Neutron Physics, Dubna, Russia*

[25]*Institute of Physics and Power Engineering, Kaluga region, Obninsk, Russia*

[26]*Istituto Nazionale di Fisica Nucleare (INFN), Laboratori Nazionali di Legnaro, Legnaro, Italy*

[27]*Centre National de la Recherche Scientifique/IN2P3—CENBG, Bordeaux, France*

[28]*Los Alamos National Laboratory, Los Alamos, New Mexico, USA*

[29]*Tokyo Institute of Technology, Tokyo, Japan*

[30]*Oak Ridge National Laboratory, Physics Division, Oak Ridge, Tennessee, USA*

[31]*NCSR, Athens, Greece*

[32]*Japan Atomic Energy Research Institute, Tokai-mura, Japan*

[33]*National Technical University of Athens, Athens, Greece*

[34]*Institut für Isotopenforschung und Kernphysik, Universität Wien, Wien, Austria*

[35]*Pôle Universitaire Léonard de Vinci, Paris La Défense, France*

[36]*CEC-JRC-IRMM, Geel, Belgium*

[37]*Department of Physics and Astronomy, University of Basel, Basel, Switzerland*

[38]*ENEA, Bologna, Italy*
[39]*Dipartimento di Fisica, Università di Bologna, and Sezione INFN di Bologna, Bologna, Italy*
(Received 13 February 2012; published 1 June 2012; publisher error corrected 20 June 2012)

The yield of the neutron capture reaction ^{232}Th(n,γ) has been measured at the neutron time-of-flight facility n_TOF at CERN in the energy range from 1 eV to 1 MeV. The reduction of the acquired data to the capture yield for resolved resonances from 1 eV to 4 keV is described and compared to a recent evaluated data set. The resonance parameters were used to assign an orbital momentum to each resonance. A missing level estimator was used to extract the s-wave level spacing of $D_0 = 17.2 \pm 0.9$ eV.

DOI: 10.1103/PhysRevC.85.064601 PACS number(s): 25.40.Lw, 25.40.Ny, 28.20.Fc, 27.90.+b

I. INTRODUCTION

The nucleus ^{232}Th plays an important role in the thorium-uranium nuclear fuel cycle [1–4] based on the fissile ^{233}U bred from ^{232}Th. The potential use of this fuel cycle is under study mainly because of its lower build-up of high-mass actinides, therefore reducing the production of radiotoxic nuclear waste, as compared to the widely used conventional uranium-plutonium fuel cycle. Accurate knowledge of cross sections of the ^{232}Th neutron-induced reactions is crucial input for the efficiently optimized design of a thorium-fuel-based nuclear system combining safe operation with the necessary power and criticality level.

Another field of interest for neutron-induced resonance reactions concerns the large parity-nonconservation effects which have been observed in neutron p-wave resonances of several isotopes including ^{232}Th [5,6]. These effects, on the order of 10^{-7} in nucleon-nucleon interactions, were found to be up to 10% in polarized neutron transmission experiments on several nuclei including ^{232}Th [7]. The asymmetries are explained as the admixing of nearby large s-wave resonances in small p-wave resonances with the same channel spin. Resonance parameters are used in the analysis of the measured asymmetries.

In general, neutron resonance data are an important calibration point for any level density model [8–10]. A careful interpretation of measured resonance data with a correction of missing levels [11,12] allows the extraction of the level density at the neutron separation energy.

The ^{232}Th(n,γ) cross sections in most of the evaluated data libraries [13] or data compilations [14,15] are based on a rather limited set of experiments [16–26] for which discrepancies have been pointed out to exist. A recent evaluation by Sirakov *et al.* [27] for neutron-induced reactions of ^{232}Th in the unresolved resonance region included in addition several recent capture measurements [28–31]. The recent release of the ENDF/B-VII.0 evaluated library [32] includes a new evaluation of ^{232}Th [33] based on a new simultaneous analysis of several resolved resonance data sets, including preliminary capture yield data from this experiment.

Neutron capture data of ^{232}Th measured with the time-of-flight technique in the resolved resonance region have often been hindered by the large radioactivity background from the high-energy γ rays of up to 2.6 MeV originating from the β decay of the daughter product ^{208}Tl. We have measured the capture cross section of ^{232}Th at the n_TOF facility at CERN where the high neutron flux per burst allowed us to strongly reduce the background due to radioactivity. The results of this measurement have been given previously for the unresolved resonance region [31]. In this paper we report the results for the resolved resonances. Since the measurement setup and data reduction procedure are the same, we only briefly describe the setup and we emphasize only the parts of the data reduction that are essential for the resolved resonances.

II. EXPERIMENTAL SETUP

The neutron-capture experiment has been performed at the n_TOF facility at CERN during phase I, before the upgrade of the spallation target [34]. A detailed description of its performances can be found elsewhere [35] and the setup used for this particular experiment has also been described previously [31].

The spallation neutrons produced with a pulsed, 6-ns wide, 20 GeV/c proton beam with up to 7×10^{12} protons per pulse in a $80 \times 80 \times 60$ cm^3 lead target are moderated by a 5.8-cm water slab surrounding the lead target. The neutron beam was obtained by means of two collimators, consisting of layers of iron and borated polyethylene. The first collimator has an inner diameter of 11 cm and an outer diameter of 50 cm and is placed 135 m from the lead target. The second collimator is located near the experimental area at a distance of 175 m and has an outer diameter of 40 cm and a variable inner diameter. For this capture experiment we used an inner diameter of 1.8 cm while for most fission experiments [36–39] a diameter of 8 cm has been used. The collimation resulted in a nearly symmetric Gaussian-shaped beam profile at the sample position of 185.2 m with a standard deviation of about 0.77 cm at low neutron energies. The spatial distribution has been accurately measured, confirming previous simulations [40], and modeled as a function of neutron energy [41].

A 1.5-T sweeping magnet placed at a distance of 145 m from the spallation target removed residual charged particles traveling along the neutron beam line. A 3-m-thick iron shielding was placed just after the magnet to remove negative muons. The neutron beam line is extended for an additional 12 m beyond the experimental area to minimize the background from back-scattered neutrons. A multifilter changer has been installed in the beam line upstream of the first collimator.

*Corresponding author:gunsing@cea.fr
†www.cern.ch/ntof

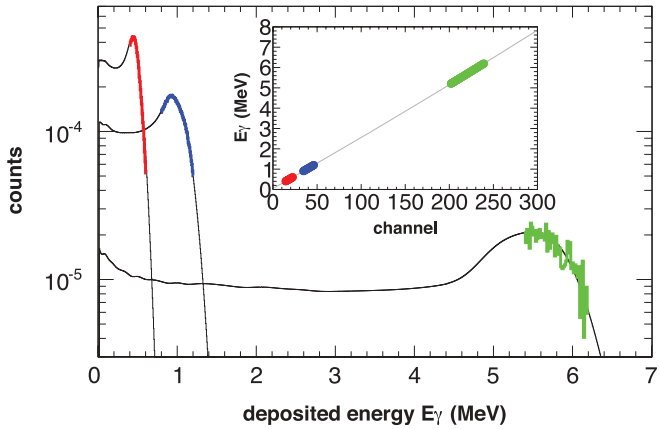

FIG. 1. (Color online) The broadened simulated spectra (in black) and part of the measured response of one detector for each of the three γ-ray sources mentioned in the text (in red, blue, and green). The simultaneously adjusted channel-energy calibration using the three response functions is shown in the inset.

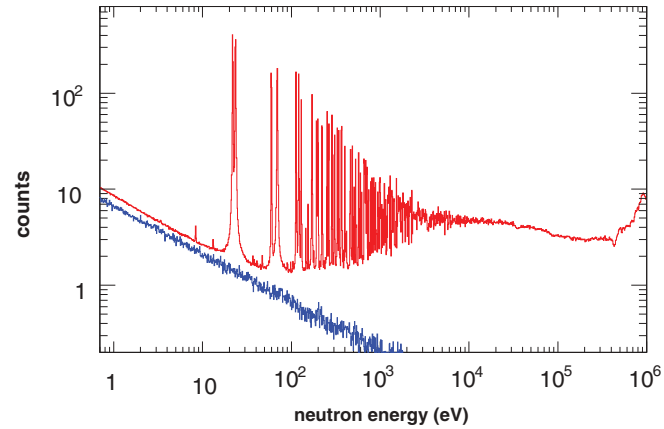

FIG. 2. (Color online) The unweighted spectrum of the thorium sample showing the resonance structure. The constant radioactive background, well below the time-of-flight spectrum, is shown in blue. In this and the following figures, counts C are expressed as counts per unit of lethargy, i.e., as $dC/d\ln E = E\,dC/dE$.

The repetition period of the proton pulses was a multiple of 2.4 s, which is long enough to cover the energy range down to subthermal energies in the experimental area at 185.2 m and to prevent overlapping of slow neutrons in subsequent cycles.

Two in-house-developed deuterated benzene C_6D_6 γ-ray detectors contained in a low-mass carbon fiber housing [42] have been used for neutron capture measurements. The samples, placed in air, were kept in position by a remotely controlled carbon fiber sample changer [43].

For the energy calibration of each C_6D_6 γ-ray detector we measured the response to radioactive sources of ^{137}Cs (0.662 MeV), ^{60}Co (1.173 and 1.332 MeV), and a composite source of ^{238}Pu with ^{13}C, giving a 6.13-MeV γ ray through the $^{13}C(\alpha, n)^{16}O^*$ reaction. With the code MCNP [44] we simulated the energy deposition in the C_6D_6 liquid scintillator volume for each of these sources. Then both the energy calibration and the Gaussian broadening of the detector response were fitted simultaneously to the regions around the Compton edge of the measured response functions, as shown in Fig. 1. This method allows us to obtain a reliable energy calibration over a large energy range.

Two disk-shaped thorium samples of 99.5% purity with a total mass of 2.8046 g and a diameter of 15 mm were placed in the beam at a flight path of 185.2 m. In addition to these samples, we used a natural lead sample to estimate the scattered photon background and a gold sample to verify the analysis procedure. All samples were fixed on thin kapton foils and mounted on the sample changer. The distance of the detectors from the center of the beam was 2.9 cm and the detectors were shifted 9.2 cm upstream from the center of the sample in order to reduce the scattered photon background.

The data-acquisition system [45] was based on Acqiris flash ADCs with 8-bit amplitude resolution and down to 1 ns sampling interval with 8 Mbytes of memory, recording for each detector its full output signal from the start time given by the incident protons. The digitizers were operated at 500 Msamples/s, allowing storage of the detector signal during a 16-ms-long time-of-flight interval, corresponding to a minimum neutron energy of 0.7 eV. After zero suppression, the data were transferred to CERN's data storage facility CASTOR for off-line analysis with dedicated pulse-shape analysis routines for each detector.

III. DETERMINATION OF THE CAPTURE YIELD

From the stored digitized detector signals, events consisting of the time of flight and the pulse height, related to the deposited energy, were extracted for each detected γ ray. These raw event data were processed to obtain the pulse-height-weighted spectra used to derive the capture yield. Only signals above the electronic threshold corresponding to 160-keV pulse height were processed further. Runs without beam served to determine the background due to the thorium activity. In order to appreciate the signal-to-background ratio we show in Fig. 2 the counting spectrum for one detector together with the background constant in time. The spectra are given as the number of counts per logarithmic bin width per nominal pulse of 7×10^{12} protons. In this way the constant background in time is visible as a decreasing line when represented as a function of the equivalent neutron energy E_n, i.e., the converted time of flight t using the relativistic time-energy relation

$$E_n = mc^2(\gamma - 1), \tag{1}$$

with $\gamma = (1 - v^2/c^2)^{-1/2}$ and $v = L/t$ and where m is the neutron mass and c the speed of light. The flight time t was calibrated for each pulse using the so-called γ flash. The flight path length L was calibrated using a measurement of the first resonance of gold. We used a measurement with gold to fit the flight path $L = 185.2$ m in combination with the resolution function. The energy of the first resonance is listed as 4.89 eV, the value which we adopted here, in ENDF/B-VII.0 and JENDL-4.0, but as 4.906 eV in JEFF-3.1 and ENDF/B-VI.8. This difference in energy scale is clearly visible at the 185.2-m flight path.

A. Weighting function

We applied the total energy method using the so-called pulsed-height-weighting technique (PHWT) to determine the number of capture reactions from the measured complex γ-ray cascade spectrum following neutron capture. This method, which is explained in considerably more detail in Ref. [46,47] and references therein, consists of using a detector with a low γ-ray efficiency so that at most one γ ray from the capture cascade is detected. Then a weight $W(E_d)$ is applied to each event with a deposited energy E_d in the detector for each detected capture event. The weights $W(E_d)$ have to be chosen in such a way that the detection efficiency ϵ_γ becomes proportional to the incident γ-ray energy E_γ,

$$\epsilon_\gamma = \int W(E_d) R_\gamma(E_d)\, dE_d = k \times E_\gamma, \tag{2}$$

where $R_\gamma(E_d)$ is the detector's response to E_γ. Then the efficiency ϵ_c of the γ-ray cascade is proportional to the cascade energy E_c as $\epsilon_c = k \times E_c$. The neutron time-of-flight spectrum $C_W(E_n)$ from the weighted counts obtained in this way becomes then

$$C_{\mathrm{W}}(E_n) = Y(E_n)\Phi(E_n) k E_c, \tag{3}$$

where $Y(E_n)$ is the capture yield and $\Phi(E_n)$ is the number of incident neutrons. The proportionality constant k is usually taken as 1 per unit of energy. The weighting function $W(E_d)$ is determined from simulated detector response functions to a series of monoenergetic γ rays. We have adjusted the parameters of a fourth-order polynomial for $W(E_d)$.

In order to account for the finite threshold of 160 keV applied in this experiment, in principle two methods can be used. One can try to estimate the missing part of the response by calculating realistic γ-ray cascades and deduce the corresponding missing detector response and correct for it [46]. The other approach (see, for example, [47] and references therein), which we have followed here, is to assume that the applied threshold is part of the detector response in the fit procedure of the weighting function.

B. Weighting function correction for the spatial distribution of γ emission

In the determination of the weighting function we simulated the detector response to monoenergetic γ rays using a homogeneous distribution of the γ rays throughout the volume of the sample. In reality, when the cross section of incident neutrons is high, as in the peaks of strong resonances, all capture reactions occur in a first thin layer of the sample. In general, the distribution of γ rays in the sample is not homogeneous but dependent on the cross section. To account for this effect, we have calculated the capture yield in the two limiting conditions, once with a weighting function derived from a homogeneous γ-ray distribution and once with a weighting function from a γ-ray distribution concentrated in a thin layer on the neutron incident side of the sample.

The maximum effect of the two extreme weighting functions for the flat part of the saturated resonances, where the layer approximation for the γ distribution holds, was a factor $a_\gamma = 0.964$ for a 160-keV threshold. Assuming a γ-ray distribution which changes across the sample axis in relation to the transmission of the neutrons through the sample, related to the total cross section σ_T and the sample thickness n, we applied the empirical correction factor already used in Ref. [47],

$$f_\gamma(E_n) = a_\gamma + (1 - a_\gamma)\exp[-n\sigma_T(E_n)], \tag{4}$$

to the neutron capture yield derived with the weighting function with the homogeneous γ-ray distribution in order to take this effect into account. This factor reflects the limiting case $f_\gamma \approx 1$ outside the the resonances where $n\sigma_T \ll 1$ and the other limit $f_\gamma \approx a_\gamma$ in the peaks of the saturated resonances where $n\sigma_T \gg 1$. In between these limits the correction factor follows the transmission $\exp(-n\sigma_T)$, which is a measure for the opacity to neutrons.

C. Dead-time correction

The use of flash ADCs for the data acquisition nearly eliminates dead time. Nevertheless, a small effective dead time on the order of a few tens of nanoseconds is present and is related to the software pulse extraction. Its effect is often negligible, except at large local count rates, like in large resonances. To estimate this effect and to correct for it, we calculated the distribution of the time differences between two consecutive events in the same time-of-flight burst, for each of the two γ-ray detectors separately. The distribution showed a nearly total suppression of the events following a previous event by less than approximately 25 ns. The same distribution but now for two consecutive events in either of the two detectors showed a pronounced peak well below 25 ns, revealing the coincidences of two γ rays of the same capture event.

In the processing of the events, we discarded all events from both detectors within a fixed time $\tau = 30$ ns after the detection of an event. In this way we counted only one of two coincident γ rays and we obtained a sharply defined dead time for which we calculated a nonextendible dead-time correction factor $f_\tau(t)$ as a function of the time of flight t as

$$f_\tau(t) = \frac{1}{1 - \frac{1}{N_b}\int_{t-\tau}^{t} S_{\mathrm{obs}}(t')\, dt'}, \tag{5}$$

where N_b is the number of time-of-flight bunches and $S_{\mathrm{obs}}(t)$ is the observed counting spectrum without event selection conditions. The correction factor, shown in Fig. 3, goes up to 1.025 in the peak of resonances in the resolved resonance region and is practically 1.0 in the valleys between them. The factor $f_\tau(t)$ derived in this way was then applied to the weighted count rate spectrum.

D. Neutron sensitivity

A recurring problem in neutron-capture measurements is the neutron sensitivity of the experimental setup. Neutrons scattering from the sample and inducing capture reactions in the detector and surrounding materials produce γ rays and contribute to the background in the detector. Since the neutron

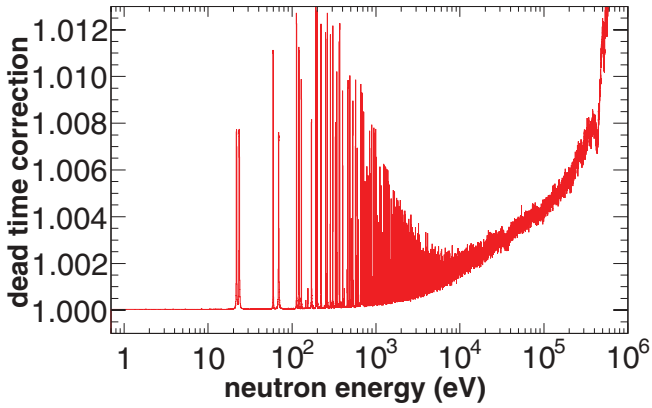

FIG. 3. (Color online) The dead-time correction factor $f_\tau(t)$ applied to the weighted time-of-flight spectrum as a function of neutron energy.

scattering cross section has the same resonance structure as the capture cross section, this special type of background in the capture yield is difficult to distinguish.

The detection probability $\epsilon_n(E_n)$ of γ rays from sample-scattered neutrons is usually measured using a sample of carbon, which has a very small and smooth capture cross section but a sizeable scattering cross section. Unfortunately, for the particular setup of this experiment, no data with a carbon sample were available. However, we had at our disposal several data sets with carbon samples which had been measured in capture experiments on other isotopes in similar setups with only slightly different detector-to-sample distances.

Therefore we performed simulations of the γ-ray detection efficiency produced by carbon-scattered neutrons, $\epsilon_n(E_n)$, in all setups and compared the results with the measured carbon data to validate the simulated $\epsilon_n(E_n)$ for the thorium experiment setup. For this we used again the code MCNP [44], assuming isotropically emitted neutrons throughout the sample volume. In addition, we simulated the detector response to the in-beam photons, also scattered from the carbon sample. The photon spectrum was available from previous simulations [48] and shows peak at time-of-flight values corresponding to the keV region. At this peak position the time-of-flight response is roughly the same for the scattered photons and the sample-scattered neutron-induced γ rays.

In the comparison of the simulated detector responses, resulting from both sample scattered neutrons and photons, and the measured carbon sample data we found a rather good agreement for neutron energies below about 10 eV, while at higher energies the agreement was within 30%. One reason for this difference may lie in the fact that the necessary detailed information on neutron capture γ-ray spectra for most nuclei is generally not available in the nuclear data libraries.

To estimate the effect as shown in Fig. 5, we have used the spectra of the energy deposit in the detector from neutrons scattered isotropically from the sample position, resulting from simulations with MCNP. From these spectra we calculated the detection efficiency $\epsilon_n(E_n)$, applying a 160-keV threshold like in the measurement and applying the weighting function we used for the thorium measurements.

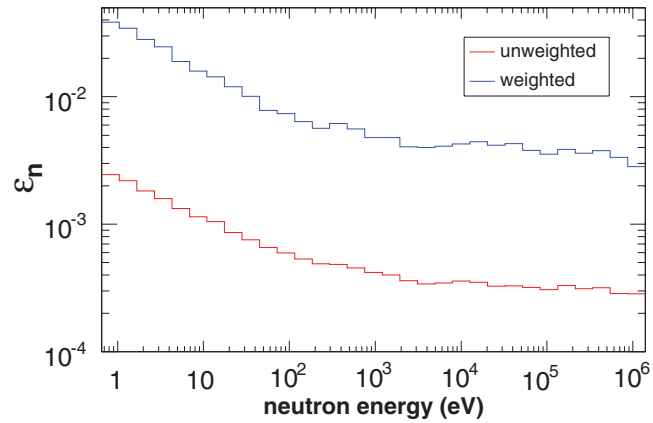

FIG. 4. (Color online) The efficiency for detecting γ rays from surrounding materials induced by sample scattered neutrons, calculated with the code MCNP [44]. The weighted efficiency includes the weighting function procedure applied to the γ rays and is not comparable to unity.

In Fig. 4 we show this efficiency with and without applying the weighting function. The unweighted response gives the detection efficiency for a single scattered neutron, while the events for weighted response had undergone the same weighting function procedure as the capture events, changing the absolute magnitude and making it therefore not comparable to unity. This weighted neutron efficiency was then multiplied by the calculated scattered neutron yield from the thorium sample and by the incident neutron flux in order to obtain the weighted count rate comparable to the capture count rate. We considered the result, shown in Fig. 5, as the contribution from sample scattered neutrons to the weighted ^{232}Th(n,γ) spectrum.

With this procedure we obtained an off-resonance contribution in the order of 10%, mainly because there the capture cross section drops to very low values while this is not the case for the scattering cross section due to potential scattering. In

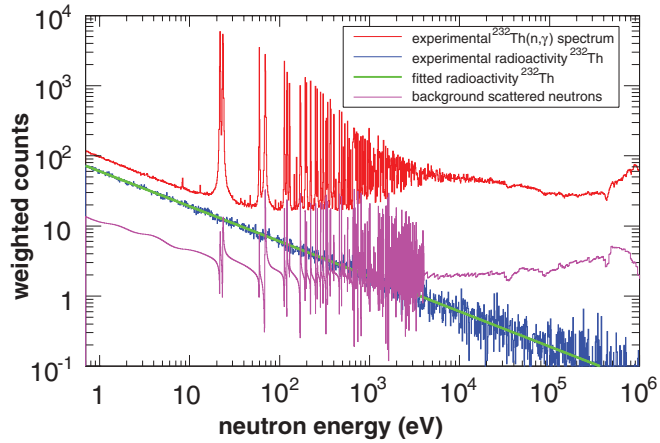

FIG. 5. (Color online) The weighted count rate spectrum of the ^{232}Th(n,γ) measurement. The estimation of the background contribution from sample scattered neutrons as obtained by Monte Carlo simulations is shown as well. For comparison also the weighted contribution of the radioactivity is shown in the figure.

the resonance region however this value is only on the order of 0.1%, since for ^{232}Th the capture cross section is much higher than the scattering cross section.

E. Neutron flux

The relative neutron flux as a function of neutron energy is needed over the energy range of interest from approximately 1 eV up to 1 MeV in order to determine the capture yield. In addition to Monte Carlo simulations [35], we have a dedicated measurement of the flux performed with a ^{235}U-loaded parallel-plate fission ionization chamber from the Physikalisch-Technische Bundesanstalt (PTB) in Braunschweig [49]. Furthermore, during the capture measurements the relative neutron flux was measured with an in-beam neutron monitor SiMon [50], consisting of a ^{6}Li deposit on a Mylar foil and four off-beam silicon detectors for the detection of the ^{6}Li$(n, ^{3}\mathrm{H})\alpha$ reaction products. Up to 1 keV both methods are in good agreement, but at higher energies the ^{6}Li(n, α) reaction suffers the insufficient knowledge of the angular distribution of the α and triton particles.

The resonance structure of the materials in the neutron beam, such as the aluminum entrance window near the spallation target, the lead of the target, and the water moderator, do not allow us to determine easily an analytical expression for the neutron flux. For example, the 337-eV resonance from ^{55}Mn present in the aluminum of the entrance window is clearly visible in the SiMon data.

The neutron flux we adopted for the capture yield is an analytical fit of the measured flux from the SiMon detectors up to 1 keV and pointwise data from the PTB measurement above this energy, suitably normalized in an overlapping energy region. Note that this flux is intended only for its energy profile and not as an absolute normalization. This adopted flux, shown in fig. 6 has been used for most of the capture measurements at n_TOF in the phase-I period [51]. The SiMon detector is still in use for the ongoing phase-II measurements together with other flux monitors. It may be possible that the angular distribution effects of the SiMon detectors will be known with more precision in the future. At present we assign an uncertainty of 2% to the shape of the flux above 1 keV.

Because the beam profile changes with neutron energy, the fraction of the neutron beam hitting the sample varies accordingly. The measured change [41] corresponds well with simulated values [40]. Since the simulations were available with higher statistics we used these to fit an empirical analytical function of the form

$$f_{\mathrm{beam}}(E_n) = b_0 E_n^{b_1} + b_2 E_n^{b_3}, \tag{6}$$

with parameters listed in Table I, and which are valid between 1 eV and 1 MeV, where the neutron beam fraction changes from 0.385 at 1 eV to 0.405 at 1 MeV as shown in Fig. 7. This analytical correction factor has been applied to the neutron flux used to calculate the capture yield.

TABLE I. Numerical values of the parameters of the modeled beam interception factor, Eq. (6).

Parameter	Numerical value
b_0	3.830698×10^{-1}
b_1	-4.134044×10^{-4}
b_2	1.060315×10^{-3}
b_3	2.292116×10^{-1}

F. Capture yield and normalization

The spectrum of the weighted detector counts was corrected for dead time, radioactive background, the spatial distribution of the γ emission in the weighting function and for sample-scattered neutrons. The corrected spectrum was then divided by the adopted neutron flux to obtain the experimental capture yield. Any remaining background needs to be included in the analysis of the resolved resonances. A normalization factor is needed in order to account for the absolute flux level and for the absolute detector efficiency.

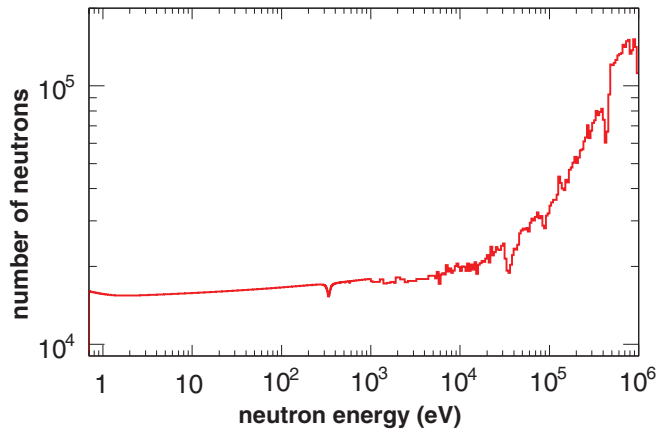

FIG. 6. (Color online) The adopted neutron flux in the energy range from 1 eV to 1 MeV at 185.2 m with the 20-mm-diameter collimator. The composition of this adopted flux is explained in the text.

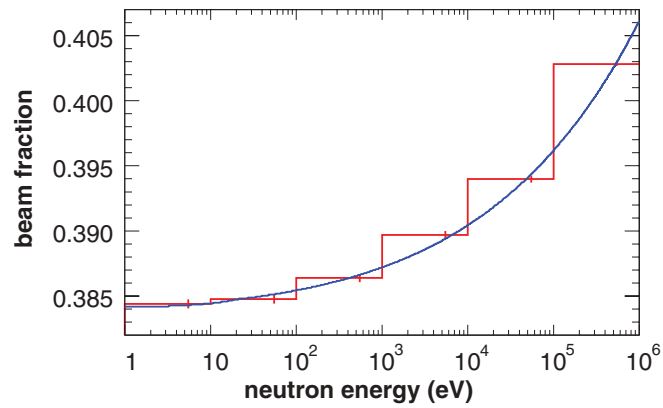

FIG. 7. (Color online) A histogram of the simulated beam interception factor, i.e., the fraction of neutrons incident on a sample, for a diameter of 1.5 cm, together with the analytical description of Eq. (6).

The normalization can be obtained if the measured cross section is known well enough in a particular energy region for the investigated nucleus or from a reference sample with a well-known cross section in the same measurement conditions. A related technique can be used with a sample thick enough to have a large macroscopic total cross section ($n\sigma_T \gg 1$) in the peak of a resonance. This results in a so-called saturated resonance where in the vicinity of the resonance peak the capture yield is not proportional to the capture cross section $n\sigma_\gamma$ but to the ratio σ_γ/σ_T, independent of the sample thickness n. This particular shape of the capture yield allows the extraction of the normalization with an R-matrix fitting code, as explained in more detail for example in Ref. [47].

In this case of the thorium sample with a thickness of 4.1×10^{-3} atoms/b, three saturated resonances of ^{232}Th were present at 21.8, 23.5, and 69.2 eV. While we could obtain a consistent value within 0.5% for the normalization from the two lower resonances depending on the fitting conditions, we could initially not reproduce the shape of the 69.2-eV saturated resonance.

The size of the applied corrections due to dead time, neutron sensitivity, and the weighting function was too small to explain the difference in shape in the saturated top of the resonance when comparing the measurement and the calculation with the code SAMMY [52]. We then simulated the expected capture yield with MCNP [44] and with GEANT4 [53], and we calculated the yield with the code REFIT [54], all using the same resonance parameters. For MCNP we have also used several calculated scattering tables [55] for this purpose, taking into account customized Doppler-broadening models, but the differences from the standard free-gas approximation for the Doppler broadening were not significant.

All codes gave similar results for the two saturated resonances at 21.8 and 23.5 eV, which we eventually used to determine the normalization. However, the results for the 69.2-eV resonance were inconsistent. The calculated yield from MCNP and SAMMY practically coincided but was different from the GEANT4 simulation result, which we considered closest to reality since no approximations were made in the scattering of the neutrons off the thermally moving atomic nuclei. The results from REFIT, which uses a simplified implementation of the scattering kernel, were closer to those of the GEANT4 simulation. In Fig. 8 we have plotted the different results, to which we added for completeness the experimental data. We concluded that both MCNP and SAMMY use approximations in the neutron scattering kernel which are often justified but not in the present case of the 69.2-eV resonance in ^{232}Th with a high capture cross section combined with a high scattering-to-capture ratio. Since then the existence of this effect has been confirmed in the 36.7-eV resonance of ^{238}U measured at Rensselaer Polytechnic Institute (RPI) [56]. Recently, Dagan has described this phenomenon in more detail and provided a workaround [57,58].

We then used the first two saturated resonances to determine the normalization factor for the capture yield. Since we used a detailed description of the geometry for the weighting function, and a neutron flux close to the absolute flux, we expect a normalization value close to unity.

The two resonances at 21.8 and 23.5 eV were fitted with the R-matrix code SAMMY [52] together with the normalization. Several combinations of free and fixed resonance parameters were used for each resonance separately and both resonances together. Since the resonances are saturated, the normalization should be independent of the resonance parameters. Indeed, a very low correlation ($\rho < 0.1$) between the normalization and the resonance parameters was found. From the various possibilities of free and fixed parameters we found normalizations consistent within 0.5%. A fit of the two resonances from which the normalization is deduced is shown in Fig. 9.

IV. RESOLVED RESONANCES

A. Doppler and resolution broadening

The shape of the resolved resonances is affected by several broadening effects. Doppler broadening is well understood and the metallic thorium samples can be described satisfactorily with the free-gas model using an effective temperature [59].

The resolution effects due to the target and moderator system are difficult to measure precisely as a function of neutron energy. The most accurate description can be obtained from Monte Carlo simulations, which need to be validated by well-known resonances. For the n_TOF resolution function two independent simulation codes have been used in the past [40,60]. More recently, new simulations have been performed with higher statistics [61], confirming the coinciding results at neutron energies below about 5 keV, but also putting into evidence deviations at higher neutron energies. In the energy interval from 1 eV to 1 MeV we adjusted the numerical results from Ref. [60] with the analytical expression (the "RPI" function) available in the R-matrix code SAMMY [52]. Both the function and its parametrization can be found in the documentation of the code.

In the R-matrix fit of resonances, an incorrect modeling of the resolution may lead to wrongly derived resonance parameters. An integral quantity such as the resonance capture integral or a Maxwellian averaged cross section is much less sensitive to incorrect resonance parameters. However,

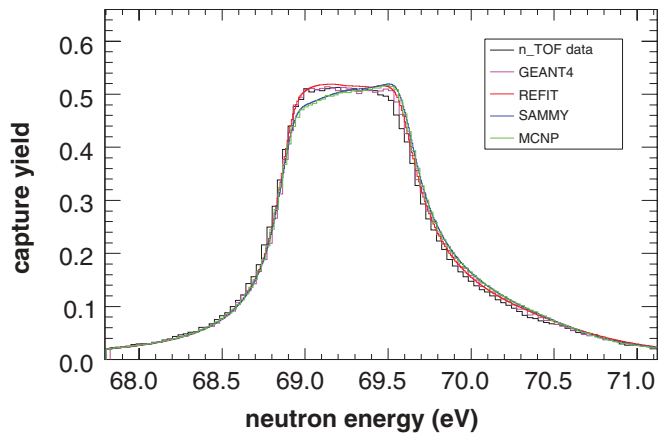

FIG. 8. (Color online) The saturated resonance at 69.2 eV calculated from the same resonance parameters with different codes, together with the experimental data.

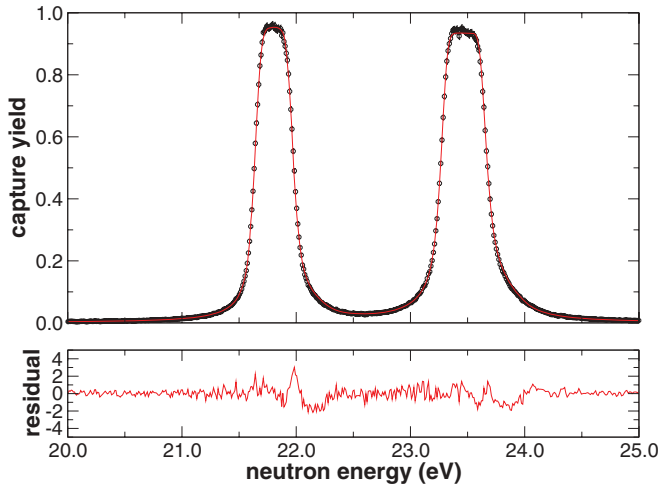

FIG. 9. (Color online) Fit and residuals for the first two s-wave resonances from which the normalization has been fitted.

if the parameters are used to calculate high-resolution cross sections with high accuracy or for example to derive strength functions or level spacings corrected for missing levels, accurate resonance parameters are needed. In addition, the resolution function is in general asymmetric, which results in a shift of the observed peak position of the resonances.

In Fig. 10 we show the components (FWHM) contributing to the observed resonance width. The Doppler broadening is the main contribution at lower neutron energies, while the resolution broadening becomes the most important contribution at higher energies. The width of the proton pulse gains importance at even higher energies. The intrinsic resonance width Γ is shown for the resonances given in the evaluated library JEFF-3.1. These widths start to be smaller than both Doppler and resolution broadening above about 60 eV. For comparison also a typical resonance spacing of 20 eV is shown in the figure. At 4 keV, where no more resolved resonances are present in the evaluated library, the resonance spacing is comparable to the combined effect of the broadening components.

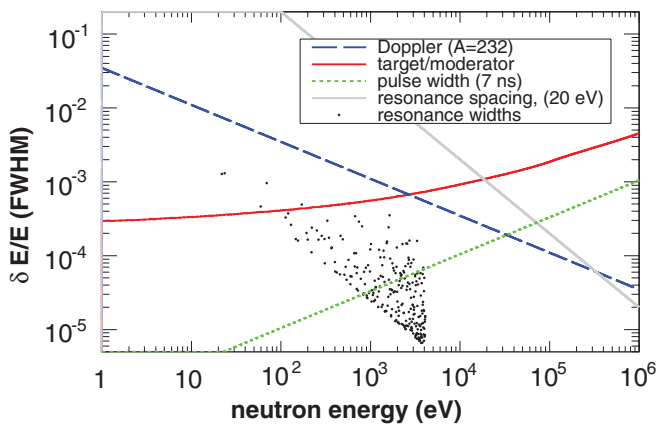

FIG. 10. (Color online) The various components contributing to the observed resonance widths.

B. Comparison with evaluated data

In Fig. 11 we plot the experimental capture yield together with the Doppler- and resolution-broadened capture yield calculated from the recent evaluation of ^{232}Th in ENDF/B-VII.0 [33]. The data are represented in 5000 bins per energy decade.

The data in Fig. 11 are corrected for the backgrounds from radioactivity, neutron sensitivity, and the time-dependent background component as described in Ref. [31], which is important especially in the unresolved resonance region. A small residual background may still be included in an R-matrix fit of the resonances.

The evaluation is based on a combined analysis of existing resonance parameters from both transmission measurements [16,22,62] and capture measurements [18,63] but also on experimental transmission data from Olsen *et al.* [22] measured at the 40-m flight path at the Oak Ridge Electron Linear Accelerator (ORELA) for eight different sample thicknesses and made available in the experimental database EXFOR, as well as a preliminary version of the present capture data, allowing a simultaneous fit of resonance parameters.

The agreement is rather good, but starting from 1 keV the agreement between the present data with the evaluated data decreases. The evaluated resonances appear slightly broader than the experimental data. This is probably because in the evaluation [33] a slightly different resolution function was chosen for the n_TOF data which allowed a better match with the ORELA data.

Unfortunately, the evaluation also includes many artificial resonances, with small p waves not contributing significantly to the capture yield but added to make the data set compatible with the statistical model. The evaluated data set can therefore not be used for a statistical level analysis. Therefore we used only the 391 experimentally observed resonances from the 919 resonances presently available in ENDF/B-VII.0. The data set given in Table II reflects only the ENDF/B-VII.0 evaluated parameters without readjustment from resonances experimentally observed in the present measurement.

While the only possible spin for s-wave resonances is $J = 1/2$, the two possible spins, 1/2 or 3/2, of the p-wave resonances are usually not known and are randomly assigned in evaluations. In the case of ^{232}Th the situation is different. From the parity nonconservation (PNC) measurements on ^{232}Th [64] nine p-wave resonances investigated up to 300 eV showed statistically significant PNC asymmetries, and these were therefore assigned a spin $J = 1/2$. This was the case for the resonances at 8.4, 38.2, 47.1, 64.6, 98.1, 128.2, 167.1, 196.2, and 232.0 eV.

V. DISCUSSION OF UNCERTAINTIES

In addition to the uncorrelated uncertainties due to counting statistics, the correlated uncertainties are important. Most of these uncertainties are described in the text. We have neglected the uncertainties due to the mass determination of the sample, dead-time correction, the correction for neutron sensitivity, and the correction from Eq. (4). The fit and subtraction of

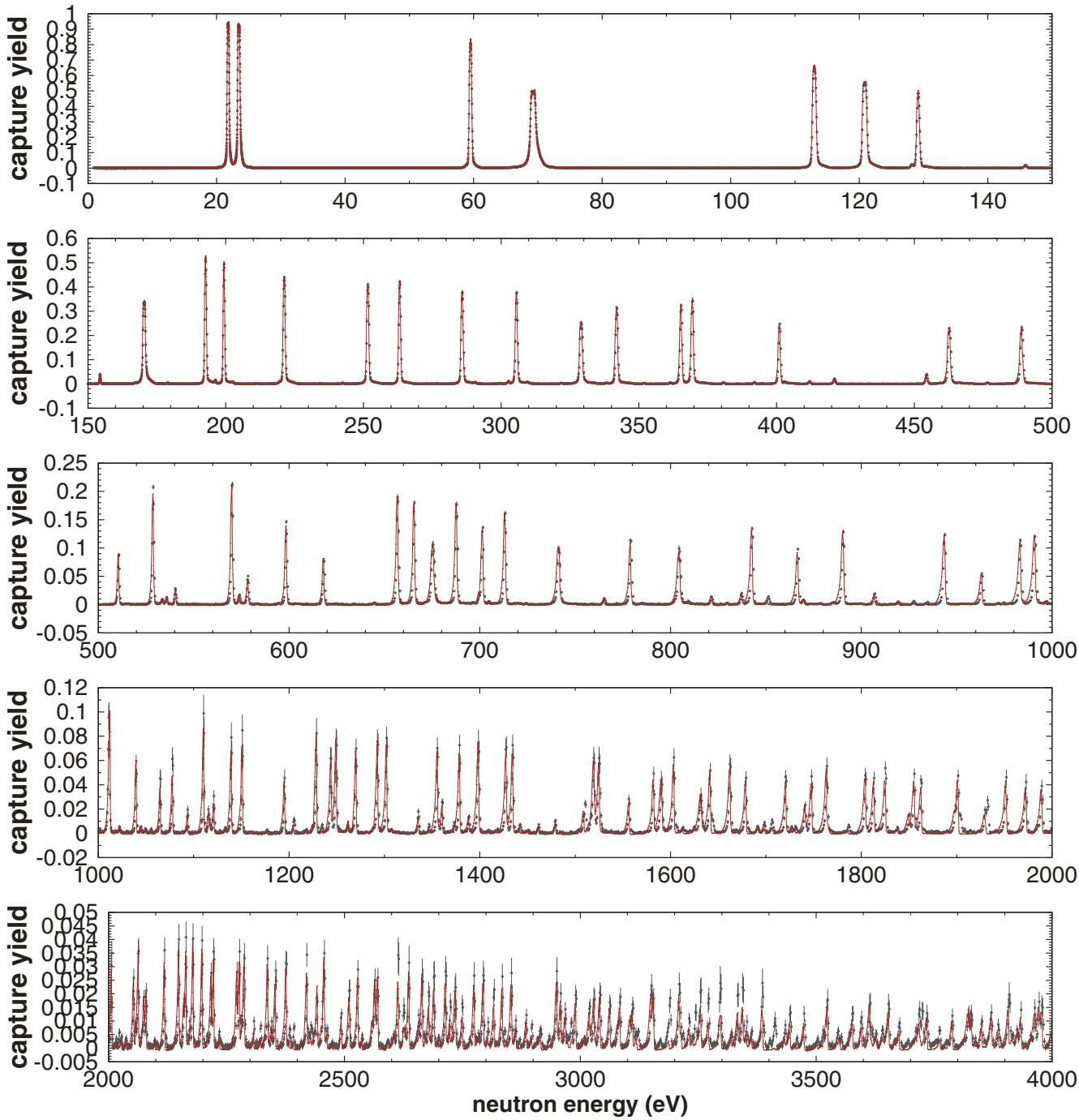

FIG. 11. (Color online) The experimental capture yield (black points) together with the capture yield calculated from evaluated data [33] including Doppler and resolution broadening (red lines). Note that the evaluation has used the present data with a slightly different resolution function than we have applied here.

the background due to the radioactivity of the sample did not introduce an uncertainty larger than 0.5%. The normalization was obtained by saturated resonances in the same sample, and therefore the total uncertainty due to the weighting function and normalization was estimated at 0.5%. The most important uncertainty comes from the energy dependence of the neutron flux, including the beam interception factor. At present, we estimate this correlated uncertainty related to the energy dependence of the flux at 2%. These uncertainties have to be taken into account in a future simultaneous R-matrix analysis of all available experimental data sets.

VI. STATISTICAL ANALYSIS OF NUCLEAR LEVELS

Resolved resonance parameters form an interesting set of closely spaced nuclear levels at a high excitation energy

TABLE II. The selected 391 resonance parameters of ^{232}Th from ENDF/B-VII.0 for resonances observed in this experiment.

E_0 (eV)	J ($\hbar$)	ℓ ($\hbar$)	Γ_γ (meV)	$g\Gamma_n$ (meV)	E_0 (eV)	J ($\hbar$)	ℓ ($\hbar$)	Γ_γ (meV)	$g\Gamma_n$ (meV)
8.36	0.5	1	24.40	0.00	13.12	1.5	1	24.40	0.00
21.81	0.5	0	25.82	2.03	23.47	0.5	0	26.76	3.77
37.01	0.5	1	24.40	0.00	38.20	1.5	1	24.40	0.00
41.03	0.5	1	24.40	0.00	47.06	1.5	1	24.40	0.00
58.79	1.5	1	24.40	0.00	59.53	0.5	0	23.76	3.78
69.24	0.5	0	23.70	42.96	90.23	0.5	1	24.40	0.01
98.06	0.5	1	24.40	0.01	113.06	0.5	0	24.22	12.78
120.89	0.5	0	23.48	21.85	128.26	1.5	1	24.40	0.04
129.21	0.5	0	30.55	3.15	145.88	0.5	0	24.40	0.09
148.07	0.5	1	24.40	0.01	154.39	0.5	0	24.40	0.21
170.42	0.5	0	24.48	59.71	192.76	0.5	0	22.96	16.00
196.28	1.5	1	24.40	0.05	199.45	0.5	0	23.23	9.54
202.70	0.5	1	24.40	0.06	211.07	1.5	1	24.40	0.01
219.55	0.5	0	24.40	0.05	221.33	0.5	0	23.98	29.25
234.29	0.5	1	24.40	0.02	242.49	1.5	1	24.40	0.03
251.69	0.5	0	24.16	30.99	258.50	0.5	1	24.40	0.02
263.28	0.5	0	22.28	21.32	272.51	1.5	1	24.40	0.01
277.02	1.5	1	24.40	0.01	285.97	0.5	0	22.88	30.34
290.62	1.5	1	24.40	0.04	302.72	1.5	1	24.40	0.08
305.69	0.5	0	22.98	28.30	309.54	0.5	0	24.43	0.06
321.90	1.5	1	24.40	0.02	329.16	0.5	0	24.26	73.76
338.14	0.5	1	24.40	0.06	342.07	0.5	0	21.56	38.02
352.01	0.5	1	24.40	0.09	361.33	1.5	1	24.40	0.05
365.44	0.5	0	21.34	25.04	369.57	0.5	0	23.01	24.65
380.77	1.5	1	24.40	0.09	391.93	0.5	1	24.40	0.18
401.19	0.5	0	22.29	10.69	402.98	0.5	0	24.40	0.14
412.03	0.5	1	24.40	0.27	421.11	0.5	0	24.40	0.55
454.59	0.5	0	24.40	1.06	458.92	1.5	1	24.40	0.03
462.85	0.5	0	22.98	62.97	466.00	0.5	1	24.40	0.08
476.55	1.5	1	24.40	0.09	489.15	0.5	0	23.03	58.07
510.76	0.5	0	24.40	3.74	528.91	0.5	0	23.33	13.96
533.65	0.5	1	24.40	0.25	536.01	1.5	1	24.40	0.21
540.65	0.5	0	24.40	1.09	550.33	1.5	1	24.40	0.04
570.25	0.5	0	22.83	27.06	573.91	1.5	1	24.40	0.31
578.62	1.5	1	24.40	0.99	584.01	0.5	1	24.40	0.03
594.50	0.5	0	24.40	0.13	598.69	0.5	0	20.93	10.62
618.34	0.5	0	27.44	4.95	644.80	1.5	1	24.40	0.08
657.12	0.5	0	23.99	47.26	665.78	0.5	0	22.27	25.52
675.70	0.5	0	23.64	207.60	688.00	0.5	0	23.06	51.52
696.05	0.5	1	24.40	0.01	700.00	0.5	0	24.40	0.50
701.63	0.5	0	27.10	13.49	704.70	0.5	1	24.40	0.35
713.41	0.5	0	22.43	27.24	720.70	0.5	1	24.40	0.10
724.98	0.5	0	24.40	0.12	741.65	0.5	0	24.16	189.94
758.59	0.5	1	24.40	0.08	765.41	1.5	1	24.40	0.36
775.08	0.5	1	24.40	0.02	779.28	0.5	0	24.40	13.37
793.78	1.5	1	24.40	0.02	804.84	0.5	0	21.83	178.06
809.51	1.5	1	24.40	0.04	821.73	1.5	1	24.40	0.61
829.81	0.5	0	24.40	0.23	837.39	0.5	0	24.40	1.47
842.96	0.5	0	24.04	26.72	850.67	1.5	1	24.40	0.17
866.92	0.5	0	21.57	14.01	870.02	1.5	1	24.40	0.38
879.27	1.5	1	24.40	0.05	885.12	1.5	1	24.40	0.18
890.76	0.5	0	23.22	38.19	900.19	1.5	1	24.40	0.05
907.15	0.5	0	24.40	1.72	919.35	1.5	1	24.40	0.24
928.27	0.5	0	24.40	0.28	934.13	1.5	1	24.40	0.19
943.93	0.5	0	23.88	46.39	955.68	0.5	1	24.40	0.06
963.42	0.5	0	22.25	7.96	974.54	1.5	1	24.40	0.10

TABLE II. (*Continued*.)

E_0 (eV)	J ($\hbar$)	ℓ ($\hbar$)	Γ_γ (meV)	$g\Gamma_n$ (meV)	E_0 (eV)	J ($\hbar$)	ℓ ($\hbar$)	Γ_γ (meV)	$g\Gamma_n$ (meV)
983.69	0.5	0	25.31	34.81	991.27	0.5	0	23.52	96.89
996.79	1.5	1	24.40	0.24	1011.31	0.5	0	23.98	121.09
1022.97	1.5	1	24.40	0.22	1029.18	0.5	1	24.40	0.03
1039.92	0.5	0	25.94	9.47	1044.80	0.5	1	24.40	0.72
1050.05	1.5	1	24.40	0.17	1055.37	1.5	1	24.40	0.24
1060.96	1.5	1	24.40	0.09	1065.29	0.5	0	25.19	6.20
1074.12	1.5	1	24.40	0.04	1078.06	0.5	0	25.27	8.66
1093.96	0.5	0	24.40	2.07	1110.75	0.5	0	23.22	27.78
1115.84	0.5	1	24.40	2.16	1117.59	1.5	1	24.40	0.35
1121.43	0.5	0	24.40	3.76	1133.41	1.5	1	24.40	0.11
1139.79	0.5	0	24.26	18.83	1151.28	0.5	0	24.18	18.96
1176.98	1.5	1	24.40	0.20	1186.77	1.5	1	24.40	0.06
1195.46	0.5	0	24.44	8.80	1204.87	1.5	1	24.40	0.46
1218.48	0.5	0	24.42	0.34	1225.66	0.5	1	24.40	0.15
1228.97	0.5	0	24.76	34.87	1234.70	0.5	1	24.40	0.31
1244.29	0.5	0	21.09	19.57	1249.87	0.5	0	23.18	127.46
1262.47	1.5	1	24.40	0.43	1262.47	1.5	1	24.40	0.43
1266.63	1.5	1	24.40	0.00	1270.55	0.5	0	26.77	21.98
1288.82	1.5	1	24.40	0.06	1293.23	0.5	0	22.88	100.53
1302.70	0.5	0	23.07	45.99	1308.01	0.5	1	24.40	0.69
1336.05	0.5	0	24.40	2.70	1346.65	1.5	1	24.40	0.33
1355.94	0.5	0	21.66	78.75	1361.06	0.5	0	24.12	5.51
1372.53	1.5	1	24.40	0.01	1379.18	0.5	0	22.46	49.01
1385.23	1.5	1	24.40	0.09	1388.81	1.5	1	24.40	1.45
1399.03	0.5	0	25.15	138.64	1409.45	1.5	1	24.40	0.14
1418.07	0.5	1	24.40	0.30	1427.96	0.5	0	22.83	112.69
1434.89	0.5	0	23.80	39.25	1441.78	0.5	0	24.40	0.94
1450.69	1.5	1	24.40	0.13	1461.91	0.5	0	24.40	1.43
1465.97	1.5	1	24.40	0.09	1479.72	0.5	0	24.40	1.95
1485.47	1.5	1	24.40	0.19	1502.57	0.5	1	24.40	0.08
1509.30	0.5	0	24.40	2.49	1509.30	0.5	0	24.40	2.49
1516.00	0.5	1	24.40	0.60	1520.07	0.5	0	23.92	200.80
1525.60	0.5	0	23.94	213.06	1556.91	0.5	0	23.75	9.14
1582.70	0.5	0	22.83	21.05	1590.93	0.5	0	24.02	361.85
1603.92	0.5	0	22.90	52.56	1613.05	0.5	1	24.40	1.08
1632.40	0.5	0	23.36	550.78	1641.92	0.5	0	25.39	32.30
1662.95	0.5	0	23.97	128.34	1679.31	0.5	0	22.15	28.38
1692.18	1.5	1	24.40	0.68	1698.73	0.5	0	24.40	2.21
1707.48	0.5	0	24.40	1.38	1721.49	0.5	0	22.85	37.38
1727.05	1.5	1	24.40	0.68	1731.00	1.5	1	24.40	0.51
1741.61	0.5	0	24.22	8.62	1748.48	0.5	0	22.92	36.55
1764.26	0.5	0	22.94	116.43	1766.60	1.5	1	24.40	0.67
1786.61	1.5	1	24.40	0.47	1793.93	0.5	1	24.40	0.00
1804.93	0.5	0	22.74	100.30	1813.69	0.5	0	23.55	34.41
1825.75	0.5	0	20.66	94.42	1838.42	1.5	1	24.40	0.50
1850.43	1.5	1	24.40	2.41	1856.04	0.5	0	24.79	35.78
1863.41	0.5	0	22.68	38.69	1890.46	0.5	0	24.40	0.25
1899.19	1.5	1	24.40	2.17	1901.95	0.5	0	22.47	88.40
1930.01	1.5	1	24.40	2.83	1931.60	0.5	0	24.40	1.43
1941.00	1.5	1	24.40	0.35	1952.23	0.5	0	22.22	115.45
1973.14	0.5	0	22.18	232.90	1989.63	0.5	0	22.46	42.10
2006.87	0.5	0	21.12	27.17	2017.07	0.5	0	24.40	0.92
2027.50	0.5	1	24.40	1.43	2038.22	0.5	0	24.40	1.32
2053.70	0.5	0	22.59	18.54	2055.76	0.5	1	24.40	0.48
2063.87	0.5	0	24.66	58.06	2075.64	0.5	0	21.98	9.93
2080.47	0.5	0	23.31	13.98	2098.89	0.5	0	24.40	0.83

TABLE II. (*Continued.*)

E_0 (eV)	J ($\hbar$)	ℓ ($\hbar$)	Γ_γ (meV)	$g\Gamma_n$ (meV)	E_0 (eV)	J ($\hbar$)	ℓ ($\hbar$)	Γ_γ (meV)	$g\Gamma_n$ (meV)
2119.09	0.5	0	19.05	77.03	2140.01	0.5	1	24.40	0.80
2149.42	0.5	0	23.68	100.91	2160.46	0.5	1	24.40	7.43
2164.85	0.5	0	22.62	83.48	2170.32	0.5	1	24.40	0.45
2179.70	0.5	0	24.91	91.65	2198.91	0.5	0	25.00	55.71
2207.06	1.5	1	24.40	0.17	2218.29	0.5	0	20.22	27.54
2223.61	0.5	0	22.95	99.92	2235.24	0.5	0	24.40	2.25
2248.09	1.5	1	24.40	0.00	2262.00	1.5	1	24.40	0.08
2272.91	0.5	0	21.67	29.12	2278.34	0.5	0	23.94	65.47
2288.20	0.5	0	23.12	305.31	2308.43	1.5	1	24.40	1.31
2313.68	1.5	1	24.40	0.04	2322.89	0.5	0	24.40	2.50
2330.75	1.5	1	24.40	0.37	2337.81	0.5	0	21.62	123.56
2345.76	0.5	1	24.40	5.06	2354.09	0.5	0	24.68	14.76
2354.09	0.5	0	24.68	14.76	2364.60	0.5	1	24.40	0.01
2377.20	0.5	0	22.86	117.46	2383.83	1.5	1	24.40	1.02
2392.78	0.5	0	24.40	1.63	2409.36	0.5	1	24.40	0.62
2414.35	1.5	1	24.40	0.05	2420.88	0.5	0	21.38	98.00
2425.66	1.5	1	24.40	0.60	2429.84	0.5	0	24.40	2.44
2438.32	1.5	1	24.40	1.17	2443.11	1.5	1	24.40	8.55
2453.62	0.5	1	24.40	1.66	2457.78	0.5	0	26.01	150.95
2463.76	0.5	0	24.40	3.30	2474.04	0.5	0	24.40	0.70
2484.51	1.5	1	24.40	0.02	2494.45	0.5	0	24.07	8.66
2511.23	0.5	0	18.40	350.24	2529.32	0.5	0	21.70	65.69
2537.51	0.5	1	24.40	2.42	2560.54	0.5	0	24.23	4.78
2565.52	0.5	0	21.78	351.95	2571.39	0.5	0	23.19	75.76
2583.19	1.5	1	24.40	0.00	2592.44	1.5	1	24.40	0.72
2605.49	1.5	1	24.40	1.37	2614.86	0.5	0	23.27	89.66
2628.16	0.5	0	23.35	5.85	2637.51	0.5	0	23.61	182.50
2655.00	0.5	1	24.40	2.29	2665.88	0.5	0	23.46	226.70
2668.30	1.5	1	24.40	0.00	2679.74	0.5	0	23.73	22.80
2690.88	0.5	0	20.90	216.26	2699.66	1.5	1	24.40	1.08
2715.46	0.5	0	23.13	89.76	2724.16	0.5	0	24.12	8.76
2736.03	0.5	0	21.79	418.24	2750.90	0.5	0	23.31	15.22
2765.91	1.5	1	24.40	0.61	2775.73	0.5	0	23.08	74.95
2784.72	0.5	1	24.40	2.45	2795.49	0.5	0	24.56	173.90
2804.72	0.5	0	24.40	3.33	2809.39	0.5	1	24.40	0.12
2817.77	0.5	0	23.42	30.54	2826.84	0.5	1	24.40	0.61
2835.31	0.5	0	23.17	52.92	2837.99	0.5	1	24.40	1.60
2854.89	0.5	0	23.15	204.51	2864.16	0.5	0	24.34	6.52
2869.58	1.5	1	24.40	0.21	2886.26	0.5	0	24.85	11.88
2898.09	0.5	0	24.07	3.89	2909.64	1.5	1	24.40	1.17
2916.74	0.5	0	24.33	5.99	2933.48	0.5	1	24.40	0.81
2944.16	1.5	1	24.40	0.93	2950.85	0.5	0	26.04	101.81
2959.25	0.5	0	20.83	43.32	2969.12	0.5	0	24.76	16.70
2974.39	1.5	1	24.40	1.05	2978.64	1.5	1	24.40	0.05
2991.10	0.5	0	24.69	38.70	2997.21	1.5	1	24.40	0.12
3009.70	0.5	0	24.40	2.16	3020.49	0.5	0	23.42	24.91
3030.06	0.5	0	20.84	247.82	3042.43	0.5	0	25.88	58.57
3063.70	0.5	0	26.32	30.30	3080.43	1.5	1	24.40	3.03
3084.99	0.5	0	23.81	38.19	3106.62	0.5	0	23.87	13.49
3111.66	0.5	0	22.39	28.36	3120.00	0.5	1	24.40	4.53
3151.47	0.5	0	21.35	143.90	3156.13	0.5	0	21.59	152.56
3169.07	0.5	0	24.40	0.26	3188.38	0.5	0	24.40	1.69
3188.38	0.5	0	24.40	1.69	3210.83	0.5	0	23.34	104.64
3215.00	1.5	1	24.40	3.30	3232.01	0.5	0	24.05	12.00
3239.85	0.5	0	24.40	2.99	3244.11	1.5	1	24.40	0.57
3256.21	0.5	0	21.50	124.29	3272.87	0.5	0	22.89	17.25

TABLE II. (*Continued.*)

E_0 (eV)	J ($\hbar$)	ℓ ($\hbar$)	Γ_γ (meV)	$g\Gamma_n$ (meV)	E_0 (eV)	J ($\hbar$)	ℓ ($\hbar$)	Γ_γ (meV)	$g\Gamma_n$ (meV)
3298.46	0.5	0	18.17	502.86	3309.26	0.5	0	24.40	0.31
3321.27	0.5	0	23.98	5.64	3335.09	0.5	0	21.30	48.28
3345.62	0.5	0	20.54	171.47	3353.39	0.5	0	24.22	9.44
3364.18	1.5	1	24.40	2.59	3387.18	0.5	0	20.20	117.94
3412.75	0.5	0	24.40	0.84	3434.25	0.5	0	23.71	6.14
3445.98	0.5	0	24.44	26.76	3458.76	0.5	0	24.40	2.46
3474.81	0.5	0	25.11	15.61	3503.58	0.5	0	24.40	2.40
3513.60	0.5	0	24.40	0.45	3524.71	0.5	0	25.40	147.71
3546.30	0.5	0	24.40	2.01	3551.07	1.5	1	24.40	3.00
3569.42	0.5	0	24.40	0.89	3578.15	0.5	0	28.23	26.20
3597.07	0.5	0	26.77	13.11	3614.87	0.5	0	26.86	184.14
3619.00	0.5	1	24.40	4.00	3628.63	0.5	0	24.06	7.84
3642.56	0.5	0	24.12	4.64	3654.88	0.5	0	27.35	78.14
3669.02	0.5	1	24.40	2.86	3677.19	0.5	0	24.71	11.69
3694.57	0.5	0	24.40	0.06	3713.09	0.5	0	24.40	4.81
3719.37	0.5	0	27.13	17.29	3722.23	0.5	0	24.38	6.97
3735.82	0.5	0	23.13	43.95	3749.76	1.5	1	24.40	0.14
3763.76	0.5	0	23.50	5.76	3778.02	1.5	1	24.40	0.00
3789.82	0.5	0	25.29	37.17	3798.13	1.5	1	24.40	0.03
3813.00	0.5	0	24.40	0.98	3823.74	0.5	0	23.78	59.12
3830.17	0.5	0	23.36	192.89	3837.76	1.5	1	24.40	1.26
3852.12	0.5	0	26.17	20.92	3859.82	1.5	1	24.40	0.24
3873.00	0.5	0	21.87	70.38	3886.96	0.5	0	24.23	17.33
3909.17	0.5	0	26.37	243.31	3917.58	0.5	1	24.40	5.31
3927.26	0.5	0	24.41	9.40	3935.36	0.5	0	25.31	47.01
3955.74	0.5	0	24.40	3.62	3964.88	0.5	0	26.08	44.37
3973.93	0.5	0	24.58	107.35	3980.03	0.5	0	29.24	169.79
4000.08	0.5	0	24.90	16.21					

just above the neutron binding energy of several MeV. The observed resonances can be analyzed within the framework of the statistical model. The distribution of level spacings and partial widths can be tested to be compatible with this model. If this is the case, such an analysis can give a reliable estimate of the level spacing D_0, an important parameter for the calibration of level density models, using the properties of the resulting distributions to correct for unobserved levels. We will compare our results with the extensive analyses in Refs. [16,65].

In the heavy compound nucleus ^{233}Th at excitation energies just above the neutron binding energy, the statistical model assumes that the matrix elements relating nuclear states are random variables with a Gaussian distribution with zero mean. This statistical model of the compound nucleus is referred to as the Gaussian orthogonal ensemble (GOE) [66–69].

The statistical model has direct consequences on the observables of the reaction cross sections. The channel widths are proportional to the square of the matrix elements and have therefore a chi-squared distribution with one degree of freedom, also known as the Porter-Thomas distribution. The observed γ width of a resonance is the sum of many (for medium and heavy nuclei several tens of thousands) individual γ widths corresponding to the decay of the capture state to each of the lower lying levels, and it tends therefore to follow a Gaussian distribution.

A. Orbital momentum assignment

In a first step we divided the resolved resonances into two groups according to their orbital momentum ℓ. Resonances with values of $\ell > 1$ have a very low expected average neutron width for ^{232}Th and are considered to be not observable. This technique, based on the difference in the penetrability factor for s and p waves, was already described by Bollinger and Thomas [70] and is explained in some detail in, for example, Ref. [11] and references therein, notably Gyulassy *et al.* [71]. The conditional probability $P(\ell=1 \mid g\Gamma_n)$ that a resonance is a p wave, given its value of $g\Gamma_n$, can be written as

$$P(\ell=1 \mid g\Gamma_n) = \left(1 + \frac{P(\ell=0)}{P(\ell=1)} \cdot \frac{P(g\Gamma_n \mid \ell=0)}{P(g\Gamma_n \mid \ell=1)}\right)^{-1}. \quad (7)$$

The probabilities $P(\ell)$ depend on the level densities $\rho_\ell = 1/D_\ell$. By using the resonance spin dependence of the level density as $\rho_\ell \propto 2J+1$, three different values are possible, depending on the target nucleus spin I, as given in Table III. The three possible values of the ratio

$$\frac{P(\ell=0)}{P(\ell=1)} = \frac{\rho_{\ell=0}}{\rho_{\ell=1}} = \frac{D_1}{D_0} \quad (8)$$

are also given in Table III. Finally, for the ratio of the probabilities $P(g\Gamma_n \mid \ell)$ for $\ell = 0$ and $\ell = 1$ we use Eq. (11)

TABLE III. Values for several quantities dependent on the target spin I as used in the text.

$I(\hbar)$	D_1/D_0	α_I	ω_I	$P_{\rm limit}$
0	1/3	1	1	3/4
1/2	4/9	2/3	3/4	9/13
$\geqslant$1	1/2	1/2	2/3	2/3

from Ref. [11] in the slightly more compact form

$$\frac{P(g\Gamma_n \mid \ell=0)}{P(g\Gamma_n \mid \ell=1)} = \frac{\sqrt{\frac{\xi}{S_0 D_0}}\exp\left[-\frac{g\Gamma_n}{2\sqrt{E}}\left(\frac{1}{S_0 D_0}-\frac{1}{\xi}\right)\right]}{\alpha_I + (1-\alpha_I)\sqrt{\frac{\pi g\Gamma_n}{2\xi\sqrt{E}}}} \quad (9)$$

using $\xi = 3\omega_I v_1 S_1 D_1$, where the values for the spin-dependent counting factors α_I and ω_I are given in Table III. S_ℓ is the neutron strength function for ℓ waves, and the factor $v_1 = \rho^2/(1+\rho^2)$ is related to the penetrability factor by $v_\ell = P_\ell(\rho)/P_0(\rho)$. The dimensionless number ρ equals ka_c, with $k = 1/\lambda\!\!\!^{-}$ being the neutron wave number and a_c the channel radius. Putting numbers in Eq. (7) results in the conditional probability that a resonance is a p-wave one. By equating in Eq. (9) the two probabilities $P(g\Gamma_n \mid \ell)$ one obtains the limit $P_{\rm limit}$, given in Table III. Resonances for which $P(\ell=1 \mid g\Gamma_n) > P_{\rm limit}$ are assigned p-wave resonances.

In Fig. 12 the value $g\Gamma_n/\sqrt{E}$ is plotted as a function of energy for the resonances and neutron widths of the $I=0$ target spin nucleus ^{232}Th listed in Table II. Solving the transcendental equation (9) gives the boundary value $g\Gamma_n/\sqrt{E}$ which divides the resonances into s and p waves. The boundary is also shown in Fig. 12. The value used for the s-wave level spacing was $D_0 = 17.2$ eV, while for the neutron strength functions we used $S_0 = 0.87\times10^{-4}$, and we used $S_1 = 1.3\times10^{-4}$ from Ref. [72]. Also shown in the figure are

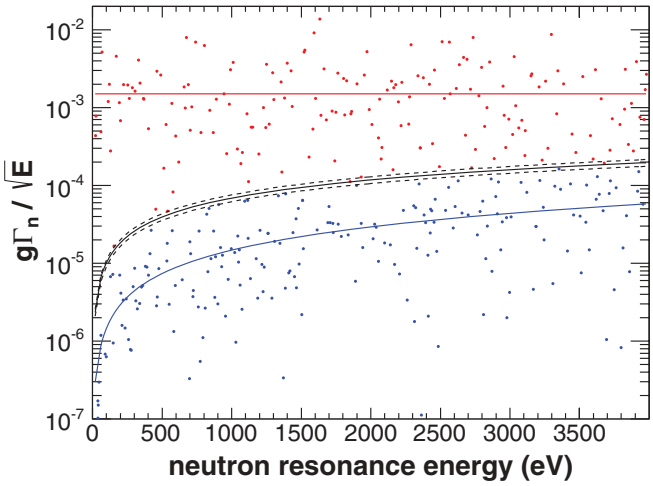

FIG. 12. (Color online) The division of the resonances in s waves (in red) and p waves (in blue). The values used are $D_0 = 17.2$ eV, $S_0 = 0.90\times10^{-4}$, $S_1 = 1.3\times10^{-4}$, and $a_c = 9.72$ fm. The effect of a 10% variation in D_0 is also shown in the figure by dashed lines. See the text for the sensitivity to other parameters.

the expectation values for the average values,

$$\langle g\Gamma_n/\sqrt{E}\rangle = (2\ell+1)v_\ell S_\ell D_\ell, \quad (10)$$

for s-wave and p-wave resonances. Once this division is made, one can use the s waves to obtain a more reliable estimate of the average level spacing D_0. Such a procedure, including a missing level correction, is less sensitive to the smaller resonances and therefore to the separation boundary between s and p waves. To illustrate this, in Fig. 12 two dashed lines around the separation boundary reflect its position if the value of D_0, and consequently the related value D_1, would increase or decrease by 10%. The sensitivities to variations in S_0, S_1, and a_c are approximately 0.2, 0.8, and 1.5 times that of D_0 in the range 1–4 keV, but these values are not shown in the figure.

B. Determination of the level spacing D_0

There are several ways to estimate the average level spacing for s waves, D_0. A first approach is to use the energy positions only in a so-called staircase plot where the cumulative number of resonances is plotted as a function of neutron energy. In the approximation of a locally constant level spacing D_0 this would result in a straight line. The Δ_3 statistic [73], reflecting the deviation of the staircase plot from a straight line, is sometimes used. Shell effects or missing levels can affect the linear trend. Since only observed resonances are taken into account, this estimate for D_0 tends to be too high. In Fig. 13 the cumulative number of resonances for both s and p waves is shown. From the s waves one can deduce as an estimate for D_0 the quantity $\Delta E/N$, the ratio of the energy interval ΔE and the number of observed resonances, N, as a function of the energy interval. This quantity is shown in the lower panel of Fig. 13 and shows a large dependence on the considered interval. This may form an indication that at this excitation energy the compound nucleus ^{233}Th cannot be fully considered within the statistical model. The obtained values are always higher than the 16.8-eV value found in Refs. [16,65], probably related to the applied division here between $\ell = 0$

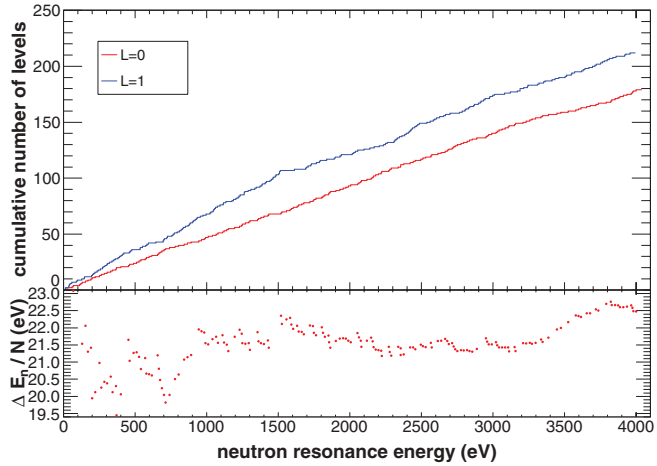

FIG. 13. (Color online) The cumulative number of observed resonances as a function of neutron energy or staircase plot (upper panel) together with the derived average level spacing.

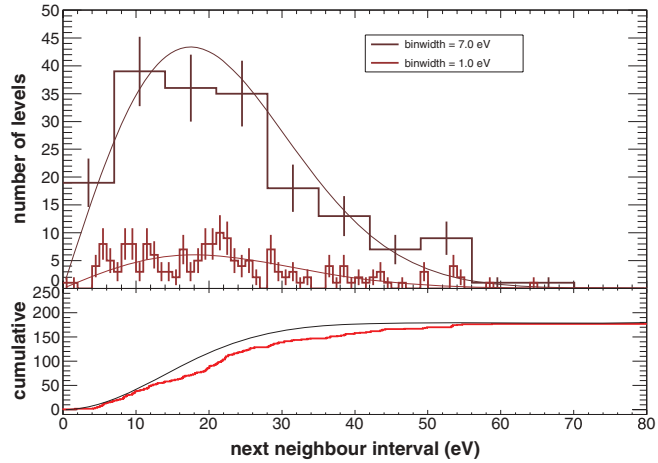

FIG. 14. (Color online) The Wigner distribution of the s-wave resonances for bin widths of 1.0 and 7.0 eV (upper panel), and the cumulative Wigner distribution (lower panel, in red). Also shown in the lower panel is the expected cumulative Wigner distribution (solid black line) for a fixed value of $D_0 = 17.2$ eV and normalized to the number of observed resonances (instead of the expected number of resonances, $\Delta E/D_0$).

and $\ell = 1$ resonances. It should be stressed that this estimate is not reliable since it does not take into account missing levels.

Another observable is the distribution of the spacing between two consecutive levels, the next-neighbor level spacing. Within the statistical model, this distribution for a spin group with the same J and ℓ is expected to be close to a Wigner distribution. The dimensionless variable $x = D_0/\langle D_0\rangle$ follows then the distribution

$$P_{\text{Wigner}}(x) = \frac{\pi}{2} x \exp\left(-\frac{\pi}{4}x^2\right). \tag{11}$$

In the upper panel of Fig. 14 a histogram of the average spacing D_0 derived from the observed ^{232}Th resonances is compared with a Wigner distribution for a fixed value of $D_0 = 17.2$ eV, using two different bin widths. The smooth curves corresponding to the Wigner distribution normalized to the bin width and the number of observed resonances follow the observed histograms, but, especially for the smaller bin width, a structure is present. A fit of such a histogram is very much dependent on the choice of binning. Therefore it may be more convenient to use the cumulative Wigner distribution instead, given by

$$P_{\text{Wigner,C}}(x) = \int_0^x P_{\text{Wigner}}(x')\,dx' = 1 - \exp\left(-\frac{\pi}{4}x^2\right), \tag{12}$$

as shown in the lower panel of Fig. 14. The expected value is normalized to the observed number of resonances, and the effect of missing levels is suggested by the deviation of the expectation value from the histogram.

A more reliable estimate of D_0 with a missing level correction also uses the neutron widths. In this approach, still based on the GOE, one estimates the number of levels, $N(x_t)$, with a reduced neutron width larger than a threshold $x_t = g\Gamma^0_{n,t}/\langle g\Gamma^0_{n,t}\rangle$ as a function of the threshold. By using the Porter-Thomas distribution of the reduced neutron widths,

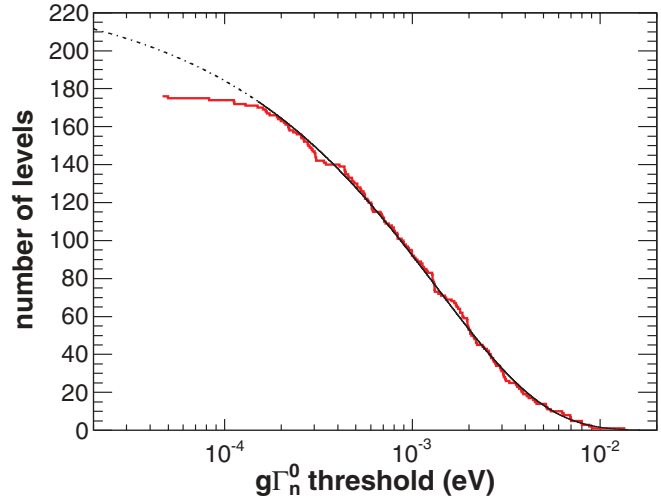

FIG. 15. (Color online) The number of observed s-wave resonances with a reduced neutron width above a threshold as a function of the threshold. The data below 1.5×10^{-4} eV are not fitted.

following from the GOE, this results in the expression

$$N(x_t) = N_0 \int_{x_t}^{\infty} \chi^2_{\nu=1}(x)\,dx = N_0(1 - \text{erf}\sqrt{x_t}), \tag{13}$$

where N_0 is the real number of resonances. This number can be fitted to the measured number of resonances above threshold. In Fig. 15 both the data and the fit are shown. The data below a limit of 1.5×10^{-4} eV are not fitted but are shown as a dashed line on the curve. The extrapolation to zero threshold yields the real number of resonances, N_0, present in the energy interval ΔE. With this procedure applied to the resonances up to 4 keV we determined $D_0 = \Delta E/N_0 = (17.2 \pm 0.9)$ eV. This number is already resulting from iterating the full procedure starting from the orbital momentum assignment with updated values for D_0. The associated uncertainty originates from repeating the procedure while varying the limit in the vicinity of 1.5×10^{-4} eV. Nevertheless, it should be noted that the obtained value is very sensitive to the applied limit and that a standard fit procedure may not be appropriate for such a highly correlated histogram.

A more complete overview of level spacing estimation can be found in Ref. [74]. We believe that for the present practical application the method described here gives the most applicable results.

C. Determination of the neutron s-wave strength function S_0

Finally, we have used the resonance parameters of the newly assigned s waves from our reduced data set to make an estimate of the neutron strength function S_0 defined by

$$S_\ell = \frac{1}{2\ell+1}\frac{\sum g\Gamma^{0,\ell}_n}{\Delta E}, \tag{14}$$

where $\Gamma^{0,\ell}_n$ is the reduced neutron width for resonances with orbital momentum ℓ. This quantity is less sensitive to missing levels than the staircase method for D_0, since missing levels are usually weak and do not contribute significantly to the sum

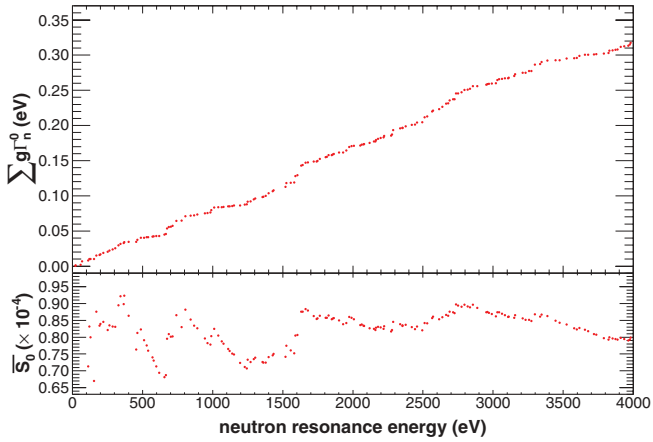

FIG. 16. (Color online) The cumulative reduced neutron width for s waves (upper panel) and the energy-averaged reduced neutron width or neutron strength function S_0 (lower panel) as a function of neutron resonance energy.

of Eq. (14). For the much weaker p waves with a much larger fraction of missing levels, this method is less applicable. In Fig. 16 the cumulative sum of the reduced neutrons widths is shown in the upper panel. The lower panel shows the estimate of S_0 as a function of the neutron resonance energy.

Up to an energy of 4 keV, an average value of $S_0 = 0.8 \times 10^{-4}$ is found, which is close to $S_0 = 0.87 \times 10^{-4}$ from Ref. [72] and to $S_0 = (0.84 \pm 0.08) \times 10^{-4}$ from Refs. [16,65]. If one observes this estimate as a function of the energy interval as shown in the lower panel of Fig. 16, it is however clear that this value is not yet stabilized and that resonance information up to higher energies may be needed. It is therefore more difficult to ascribe a firm value for the uncertainty of S_0.

VII. CONCLUSION

In the present work the measurement of the yield of the ^{232}Th(n,γ) reaction at the n_TOF facility at CERN is described. This yield, which will be submitted to the EXFOR database, can be used for future evaluations. A combined R-matrix fit with other experimental capture yields and transmission data, as done in Ref. [33], is the preferred way to obtain resonance parameters. Using our data set, we have reduced the number of resonances in the ENDF-B/VII.0 evaluation to only experimentally observed resonances. The resolved resonance data have been analyzed within the statistical model. A separation in s and p waves, as well as the level spacing D_0, and the neutron s-wave strength function S_0 have been extracted.

ACKNOWLEDGMENTS

This work has been supported by the European Commission's 5th Framework Programme under Contract No. FIKW-CT-2000-00107 (n_TOF-ND-ADS Project). The authors would like to thank R. Dagan from KIT for his help with MCNP in relation to Doppler broadening.

[1] S. David *et al.*, Nucl. Instrum. Methods Phys. Res., Sect. A **443**, 510 (2000).
[2] A. Bidaud, Ph.D. thesis, University Paris XI, Orsay, 2005.
[3] IAEA Technical Report, Thorium Fuel Cycle—Potential Benefits and Challenges, IAEA TECDOC 1450, May 2005 [http://www-pub.iaea.org/MTCD/Publications/PDF/TE_1450_web.pdf] (unpublished).
[4] Thorium Report Committee, Thorium as an Energy Source—Opportunities for Norway, Tech. Rep., January 2008 [http://www.regjeringen.no/upload/OED/Rapporter/ThoriumReport2008.pdf] (unpublished).
[5] G. E. Mitchell, J. D. Bowman, and H. A. Weidenmüller, Rev. Mod. Phys. **71**, 445 (1999).
[6] E. I. Sharapov *et al.*, Phys. Rev. C **61**, 025501 (2000).
[7] S. L. Stephenson *et al.*, Phys. Rev. C **58**, 1236 (1998).
[8] T. von Egidy and D. Bucurescu, Phys. Rev. C **72**, 044311 (2005).
[9] H. Nakamura and T. Fukahori, Phys. Rev. C **72**, 064329 (2005).
[10] W. P. Abfalterer, R. W. Finlay, and S. M. Grimes, Phys. Rev. C **62**, 064312 (2000).
[11] F. Gunsing *et al.*, Phys. Rev. C **61**, 054608 (2000).
[12] U. Agvaanluvsan *et al.*, Nucl. Instrum. Methods Phys. Res., Sect. A **498**, 459 (2004).
[13] See, for example, the International Atomic Energy Agency [www-nds.iaea.org] or the OECD Nuclear Energy Agency [www.nea.fr].
[14] S. I. Sukhoruchkin, Z. N. Soroko, and V. V. Deriglazov, *Low Energy Neutron Physics, Volume I/16B, 16C, Tables of Neutron Resonance Parameters* (Springer, Landolt-Börnstein, 1998, 2004).
[15] S. F. Mughabghab, *Atlas of Neutron Resonances* (Elsevier, Dordrecht, 2005).
[16] F. Rahn *et al.*, Phys. Rev. C **6**, 1854 (1972).
[17] M. Lindner, R. J. Nagle, and J. H. Landrum, Nucl. Sci. Eng. **59**, 381 (1976).
[18] R. L. Macklin and J. Halperin, Nucl. Sci. Eng. **64**, 849 (1977).
[19] W. P. Poenitz and D. L. Smith, Argonne National Laboratory, Technical Report ANL/NDM-42, 1978 (unpublished).
[20] K. Kobayashi, Y. Fujita, and N. Yamamuro, J. Nucl. Sci. Techn. **18**, 823 (1981).
[21] R. L. Macklin, Nucl. Sci. Eng. **79**, 118 (1981).
[22] D. K. Olsen, R. W. Ingle, and J. L. Portney, Nucl. Sci. Eng. **82**, 289 (1982).
[23] R. B. Perez *et al.*, Nucl. Sci. Eng. **80**, 189 (1982).
[24] K. Kobayashi *et al.*, Ann. Nucl. Energ. **15**, 381 (1988).
[25] W. Y. Baek *et al.*, Nucl. Instrum. Methods Phys. Res., Sect. B **168**, 453 (2000).
[26] Y. V. Grigoriev *et al.*, J. Nucl. Sci. Technol. Suppl. **2**, 350 (2002).
[27] I. Sirakov *et al.*, Ann. Nucl. Energy **35**, 1223 (2008).
[28] A. Borella *et al.*, Nucl. Sci. Eng. **152**, 1 (2006).
[29] K. Wisshak, F. Voss, and F. Käppeler, Nucl. Sci. Eng. **137**, 183 (2001).
[30] D. Karamanis *et al.*, Nucl. Sci. Eng. **139**, 282 (2001).
[31] G. Aerts *et al.* (n_TOF Collaboration), Phys. Rev. C **73**, 054610 (2006).

[32] M. B. Chadwick *et al.*, Evaluated Nuclear Data File ENDF/B-VII.0 , Nucl. Data Sheets **107**, 2931 (2006).
[33] H. Derrien, L. C. Leal, and N. M. Larson, Nucl. Sci. Eng. **160**, 149 (2008).
[34] E. Chiaveri *et al.*, J. Korean Phys. Soc. **59**, 1620 (2011).
[35] U. Abbondanno *et al.*, CERN Technical Report CERN-SL-2002-053 ECT, 2003 (unpublished).
[36] F. Belloni *et al.*, Eur. Phys. J. A **47** (2011).
[37] C. Paradela *et al.*, Phys. Rev. C **82**, 034601 (2010).
[38] D. Tarrio *et al.*, Phys. Rev. C **83**, 044620 (2011).
[39] R. Sarmento *et al.*, Phys. Rev. C **84**, 044618 (2011).
[40] V. Vlachoudis. (private communication).
[41] J. Pancin *et al.*, Nucl. Instrum. Methods Phys. Res., Sect. A **524**, 102 (2004).
[42] R. Plag *et al.*, Nucl. Instrum. Methods Phys. Res., Sect. A **496**, 425 (2003).
[43] P. M. Milazzo *et al.*, Nucl. Instrum. Methods Phys. Res., Sect. B **213** (2004/1).
[44] J. F. Briesmeister, MCNP—A General Monte Carlo *N*-Particle Transport Code, Version 4C3, 2000.
[45] U. Abbondanno *et al.*, Nucl. Instrum. Methods Phys. Res., Sect. A **538**, 692 (2005).
[46] J. L. Tain *et al.*, J. Nucl. Sci. Technol. Supplement **2**, 689 (2002).
[47] A. Borella *et al.*, Nucl. Instrum. Methods Phys. Res., Sect. A **577**, 626 (2007).
[48] A. Ferrari, C. Rubbia, and V. Vlachoudis, CERN Technical Report CERN-SL-EET-2001-036, 2002 (unpublished).
[49] C. Borcea *et al.*, Nucl. Instrum. Methods Phys. Res., Sect. A **513**, 524 (2003).
[50] S. Marrone *et al.*, Nucl. Instrum. Methods Phys. Res., Sect. A **517**, 389 (2004).
[51] F. Gunsing *et al.*, Nucl. Instrum. Methods Phys. Res., Sect. B **261**, 925 (2007).
[52] N. M. Larson, computer code SAMMY version 8, Oak Ridge National Laboratory Report ORNL/TM-9179/R7, 2006.
[53] J. Allison *et al.*, IEEE Trans. Nucl. Sci. **53**, 270 (2006).
[54] M. C. Moxon and J. Brisland, computer code REFIT, United Kingdom Atomic Energy Authority, Harwell, UK, 1991.
[55] R. Dagan (private communication).
[56] T.-I. Ro *et al.*, J. Korean Phys. Soc. **55**, 1389 (2009).
[57] R. Dagan, Ann. Nucl. Eng. **35**, 1109 (2008).
[58] R. Dagan *et al.*, J. Korean Phys. Soc. **59**, 983 (2011).
[59] W. E. Lamb, Phys. Rev. **55**, 190 (1939).
[60] C. Coceva *et al.*, Nucl. Instrum. Methods Phys. Res., Sect. A **489**, 346 (2002).
[61] C. Carrapico, Nucl. Technology **168**, 837 (2009).
[62] P. Ribon, Ph.D. thesis, University of Orsay, France, 1969.
[63] L. Forman *et al.*, in *Proceedings Third Conference on Neutron Cross Sections and Technology, Knoxville, Tennessee*, Vol. 2 (National Technical Information Service, US Dept. of Commerce, Springfield, Virginia, 1971), p. 735.
[64] S. L. Stephenson *et al.*, Phys. Rev. C **58**, 1236 (1998).
[65] H. I. Liou, H. S. Camarda, and F. Rahn, Phys. Rev. C **5**, 1002 (1972).
[66] J. E. Lynn, *The Theory of Neutron Resonance Reactions* (Clarendon, Oxford, 1968).
[67] O. Bohigas, M. J. Giannoni, and C. Schmit, Phys. Rev. Lett. **52**, 1 (1984).
[68] M. L. Mehta, *Random Matrices* (Academic, New York, 1991).
[69] H. A. Weidenmüller and G. E. Mitchell, Rev. Mod. Phys. **81**, 539 (2009).
[70] L. M. Bollinger and G. E. Thomas, Phys. Rev. **171**, 1293 (1968).
[71] M. Gyulassy, R. J. Howerton, andS. T. Perkins, Lawrence Livermore National Laboratory Technical Report UCRL-50400, 1972 (unpublished).
[72] E. S. Soukhovitskii, R. Capote, J. M. Quesada, and S. Chiba, Phys. Rev. C **72**, 024604 (2005).
[73] F. J. Dyson and M. L. Mehta, J. Math. Phys. **4**, 701 (1963).
[74] G. E. Mitchell and J. F. J. Shriner, International Atomic Energy Agency Technical Report INDC(NDS)-0561, 2009 (unpublished).